Acta Geotechnica
https://doi.org/10.1007/s11440-024-02288-x

RESEARCH PAPER

Acid-assisted subcritical blunt-tip crack propagation in carbonate rocks

XiaoJie Tang[1] · ManMan Hu[1]

Received: 22 June 2023 / Accepted: 3 February 2024

Abstract

Subcritical crack propagation in stressed carbonate rocks in a chemically reactive environment is a fundamental mechanism underlying many geomechanical processes frequently encountered in the engineering of geo-energy, including unconventional shale gas, geothermal energy, carbon sequestration and utilization. How a macroscopic Mode I crack propagates driven by a reactive fluid pressurizing on the crack surfaces with acidic agents diffusing into the rock matrix remains an open question. Here, the carbonate rock is modeled as an elasto-viscoplastic material with the mineral mass removal process affecting the rock properties in both elastic and plastic domains. A blunt-tip crack is considered to avoid any geometrically induced singularity problem and to allow a numerical analysis on the evolution of the chemical field being linked to the micro-cracking activities in front of the crack tip, affecting the delivery of acid. The model is capable of reproducing an archetypal three-region behavior of subcritical crack growth in a reactive environment. The crack propagation exhibits a prominent acceleration in Region III due to a two-way mutually enhancing feedback between mineral dissolution and the degradation process, which is most pronounced in front of the crack tip. With the consideration of initial imperfections in the rock, the macroscopic crack propagation is further accelerated with a secondary acceleration arising due to self-organization of micro-bands inside the chemically enabled plasticity zone.

Keywords Reactive environment · Micro-cracking · Acid enhancement · Stress intensity factor · Chemical softening · Self-organization

List of symbols

$\dot{\varepsilon}_{ij}^{\mathrm{el}}, \dot{\varepsilon}_{ij}^{\mathrm{pl}}$	Elastic (reversible) and plastic (irreversible) part of the strain rate
E_{ijkl}	Elasticity tensor
σ_{ij}	Stress tensor
ξ^{REV}	Integrated mineral mass removal in a representative elementary volume (REV)
ξ^{loc}	Integration of local chemical mass removal
$\dot{\xi}^{\mathrm{REV}}$	Mineral dissolution rate at REV-scale
$\dot{\xi}^{\mathrm{loc}}$	Mineral dissolution rate at local scale
$\partial f/\partial\sigma_{ij}$	Yield locus gradient
$\dot{\lambda}$	Magnitude of plastic strain rate
$\langle\bullet\rangle$	Macaulay brackets
$\dot{\varepsilon}_{\mathrm{q}}^{\mathrm{pl}}, \dot{\varepsilon}_{\mathrm{v}}^{\mathrm{pl}}$	Deviatoric and volumetric components of the plastic strain rate
$\dot{\varepsilon}_{\mathrm{ref}}$	Reference strain rate
q, p'	Equivalent deviatoric stress and the volumetric mean effective normal stress
$Y_{p',q}$	The normal or deviatoric component of the reference yield stress without any chemical dissolution
$\beta_q, \beta_{p'}$	Coefficients representing the effect of mass removal on the deviatoric and normal components of the yield limit
$\hat{\varepsilon}$	Strain invariant acting as a proxy for local mechanical damage
η	Coefficient of microcracking enhancement on the process of chemical dissolution
$x_{\mathrm{Ca}^{2+}}$	Molar fraction of calcium

✉ ManMan Hu
mmhu@hku.hk

[1] Department of Civil Engineering, The University of Hong Kong, Hong Kong, Hong Kong SAR, China

Published online: 11 March 2024

β_{H^+}	Lumped constant representing a combined effect of local acidity and damage enhancement on the mass dissolution rate
k'	Exponential index
$D_{Ca^{2+}}$	Diffusivity of calcium
D_{H^+}	Diffusivity of hydrogen
γ_{CH}	Proportionality constant of the concentration change rate of hydrogen due to consumption over the mass transfer rate of calcium production in the REV
C_{H^+}	Local hydrogen concentration
$L_{ref}, \sigma_{ref}, C_{ref}, t_{ref}$	Reference values for displacement, stress, concentration and time, respectively
t	Time
E_0	Initial Young's modulus
υ	Poisson's ratio
k	Yield stress
c_0	Initial rock cohesion
p_{in}	Fluid pressure applied on both the crack surfaces and the tip
p_{ex}	Confining pressure applied on the exterior of the process zone
C_a	Hydrogen concentration imposed at the cavity boundary
a, b	Radius of the round-tip of the blunt crack and the size of the process zone
σ_r, σ_θ	Radial and circumferential stress components
u_a	Movement of the crack tip point

1 Introduction

To meet the increasing energy demand world-widely, hydrocarbon exploitation of unconventional reservoirs undergoes rapid development toward a commercial scale in recent years. Unconventional oil and gas reservoirs in general refer to those tight rock formations characterized by very low permeability, for which the bearing hydrocarbon resources can hardly be extracted at economic flow rates without the assistance of a suitable stimulation treatment [38]. Together with the development of horizontal drilling, hydraulic fracturing (i.e., fracking) has become a common technique for the subsurface exploitation of unconventional oil and gas reservoirs. The process of fracking typically involves injection of a highly pressurized fluid into the target bedrock to create a network of cracks and hence sufficient fluid pathways. For those unconventional reservoirs containing rich carbonate, the acidizing treatment is often incorporated to chemically soften the host rock. The predominant chemical reaction occurring in a carbonate under weak acid assisted fracturing can be described by Eq. (1) [46]:

$$CaCO_3(s) + H^+(aq) \leftrightarrow Ca^{2+}(aq) + HCO_3^-(aq) \quad (1)$$

When in-situ chemical weakening is at play in the rock formation, a reduced hydraulic pressure is required and cracks propagate at a subcritical regime [3]. A proper understanding of acid–water–rock interactions is of critical importance to the optimization of acidizing-assisted hydraulic fracturing in terms of operational cost and well productivity, as well as the environmental safety. This calls for an in-depth investigation into the evolving interplay between the constitutive behavior, including both the elastic and plastic domain [9, 26, 27], of a degrading geomaterial and the chemically reactive environment it is subject to. In particular, how a single macroscopic crack propagates with fluid pressurizing on the crack surface in tandem with mineral mass removal occurring around the propagating front remains an open question.

Studies on tensile (Mode I) crack propagation in solids date back to the classical Griffith's criterion [18] based on energy balance for linear elastic brittle materials and Irwin's modification [30] to account for the crack-tip plasticity accompanied by dissipation of heat. An energetic path-independent contour integral is widely adopted to calculate the fracture toughness from far-field avoiding the stress-field singularity problem associated with the crack tip, which is often referred to as the *J*-integral, after Rice [39]. Notable extension of the *J*-integral concept as applied to tensile cracking includes theoretical investigations focusing on e.g. energy flow during elastic crack extension [5, 16], elastoplasticity of a hardening material [28], rheological behavior of viscoelastic materials [40] and interfacial crack growth of anisotropic bimaterials [37]. Abundant laboratory evidences have revealed that the stress intensity factor derived from the *J*-integral representing the fracture toughness in a brittle solid during propagation is correlated to the logarithmic of crack velocity following a linear trend in non-reactive environments [8, 47]. For a reactive environment, for instance in the presence of water, vapor, or fluid carrying acidic agents, stress corrosion in the vicinity of the propagating crack tip plays a role. The experiment presented by Atkinson and Meredith [4] investigates the influence of fluid acidity on the tensile cracking velocity in synthetic quartz specimens, which demonstrates that the chemical enhancement on crack propagation is proportional to the pore water activity of the imposed aqueous environment.

The underlying mechanism of dynamic crack growth in quartz is believed to be a microscopic picture pertinent to bond-rupture that is induced chemically or mechanically (or both, in a coupled manner) depending on the crack propagation velocity and the time scales defining the reaction–diffusion processes [15, 47].

For acid-assisted subcritical crack propagation in carbonates, while Hu and Hueckel offer a general semi-analytical formulation [27] extending the Airy stress function [1] to account for induced chemical softening in rocks, this contribution aims to provide a numerical platform that investigates the growth of a single fracture under combined mechanical and chemical loads, capturing the three-region crack propagation behavior as an archetype response of Mode I cracking immersed in a reactive environment. It has been noted that both chemical dissolution (and possible re-precipitation) and micro-plasticity around the crack tip play important roles in the geological setting of subcritical crack growth [3]. Indeed, a mineral mass removal from a solid affects the mechanical strength causing degradation of the material. When the time scale defined by the spontaneous or triggered mineral mass flux is comparable to the counterpart by the mechanical process (e.g. crack propagation in the current study), multiphysics feedback is expected to pronounce [22]. Laboratory evidence has shown that the constitutive behavior of calcarenites in the presence of acidic environment is affected by the progress of chemical reaction indicated by mass removal content, in both oedometric and triaxial tests [10–12]. Microscopically, it is observed that micro-cracking occurs at the stressed intergranular contact in, for instance, pressure solution and sedimentary aging [19, 20, 45], providing additional sites for chemical dissolution [6, 26]. The concept of coupled chemo-plasticity thereby links chemical softening to the extent of micro-cracking and the associated irreversible dilatancy, the increase of the total specific surface area and hence the increase in mineral dissolution [21, 26].

Rocks, as a natural geological material, are inherently heterogeneous. While classical analytical solutions assuming in general homogeneity provide an important baseline for the evolution of stress and deformation field during crack growth, here we deploy a numerical experimentation on investigating the role that rock heterogeneity plays in advancing the propagation of a single crack in a chemically reactive environment. Studies on the effect that heterogeneity, manifested as a spatial fluctuation of material properties, poses on the emergence of shear banding in soils and rocks prior to failure have been enabled by numerical approaches in recent years [29, 32]. The spatial heterogeneity in terms of density variation has been confirmed to be a determining factor for shear localization to appear in a geomaterial under compressive loading. Variability in local mechanical properties originating from the intrinsic heterogeneity of a geomaterial is suggested to be a major factor influencing the global behavior and the onset of bifurcation [41]. Heterogeneous microstructure of claystones is taken into account by Pardoen et al. [33] by assigning different values of elastic modulus to various mineral constituents. Further attempts have been made on mapping the local material properties through non-invasive laboratory techniques such as X-ray tomography measurements into continuum-based numerical methods for analyzing the formation of shear bands [13, 42]. However, the influence of intrinsic rock inhomogeneity on Mode I crack propagation considering reactive environments has not been explored so far.

The current study presents a numerical investigation on the propagation of a single macroscopic crack in a chemical environment, employing a reactive-visco-plasticity model recently proposed by Tang and Hu [46] based on the phenomenon of chemical ductilization observed in calcarenite tests in post-yield regimes [10, 11]. Sensitivity studies on the role of the imposed chemical environment as well as the susceptibility of the rock in the presence of acidity to microcracking are carried out, followed by an investigation into the propagation of crack incorporating the consideration of inhomogeneity modeled as spatial fluctuation in the initial distribution of the mass removal field. The paper is organized as follows. Section 2 presents the numerical setup for a blunt-tip macroscopic crack undergoing subcritical propagation and formulates the framework of the coupled chemo-mechanics aiming at providing such a basis that the intricate interactions between solid matrix deformation, chemical reaction and solute transport in the process zone are captured. The governing equations describing a multiphysics involved system are implemented into an open-source simulator based on the MOOSE environment benchmarked against the slip-line field solution of an axisymmetric deformation, as detailed in Sect. 3. The numerical results of a two-dimensional acid-assisted crack propagation problem are presented and analyzed in Sect. 4.

2 Model description

In order to investigate the subcritical crack propagation in a carbonate rock undergoing chemical degradation, a suitable model should address the chemical alteration on the rock constitutive behavior and meanwhile the effect of rock deformation on the chemical environment. In what follows, we describe such a conceptual model where the mechanical behavior of the rock is dependent on the progress of the chemical dissolution, which is linked to the reactive transport in the aqueous phase being affected by the micro-

cracking process via mass balance. A two-way chemo-mechanical feedback is thereby established, which is considered as a necessity for modeling the archetypal tensile crack propagation behavior spanning characteristic three regions as observed in the laboratory.

2.1 Constitutive considerations for carbonate rocks in a reactive environment

The constitutive considerations are based on a series of laboratory experiments on calcarenite specimens exposed to reactive environments [10–12]. It is observed that the rock behavior is controlled by the variable of reaction progress (the integrated mass removal) in terms of both plastic and elastic properties. Also, a chemically enabled ductilization in the post-yield regime is noted, as the stressed rock undergoes chemical softening due to the progressive loss of mineral mass. In the current study, a carbonate rock subject to concurrent deformation and induced internal mass exchange is modeled as an elasto-visco-plastic material with both the reversible and irreversible portions of the strain chemically-affected.

2.1.1 Reactive chemo-elasticity of carbonate rocks

For the elastic portion of deformation, the chemical influence is implemented into the elastic modulus following the coupled chemo-elasticity [27], where the elasticity tensor E_{ijkl} is defined as dependent on a local chemical quantity ξ^{loc}.

$$\sigma_{ij} = E_{ijkl}\left(\xi^{\mathrm{loc}}\right) \cdot \varepsilon_{kl}^{\mathrm{el}} \tag{2}$$

where σ_{ij} and $\varepsilon_{kl}^{\mathrm{el}}$ denote the stress tensor and the elastic (reversible) part of the strain, respectively. ξ^{loc} denotes a scalar variable representing the integration of local mineral mass removal over time:

$$\xi^{\mathrm{loc}}(t) = \int_0^t \dot{\xi}^{\mathrm{loc}} \mathrm{d}\tau \tag{3}$$

where $\dot{\xi}^{\mathrm{loc}} = \mathrm{d}\xi^{\mathrm{loc}}/\mathrm{d}\tau$ denotes the rate of the local mass removal.

In analogy to the classical concept of thermo-elasticity, where the elastic modulus exhibits a dependence on the thermal field, Eq. (2) in the context of the rock elastic response being affected by a chemical field is interpreted as follows. The chemical mass removal from a solid at constant stress via mineral dissolution produces an instantaneous strain in addition to the pure mechanical strain, manifesting as a change in the magnitude of the effective Young's modulus. Note that the chemically induced shrinkage via mineral dissolution is assumed as isotropic within this chemo-elasticity regime. A linear dependence of the elasticity modulus on the progress of chemical mass removal is assumed in this study for simplicity.

2.1.2 Reactive chemo-visco-plasticity of carbonate rocks

For the irreversible portion of the deformation, we follow the strategy proposed by Tang and Hu [46], where the magnitude of the plastic strain rate $\dot{\lambda}$ is expressed through deviatoric and volumetric components:

$$\dot{\lambda} = \sqrt{\dot{\varepsilon}_q^{\mathrm{pl2}} + \dot{\varepsilon}_v^{\mathrm{pl2}}} \tag{4}$$

where $\dot{\varepsilon}_q^{\mathrm{pl}}$ and $\dot{\varepsilon}_v^{\mathrm{pl}}$ represent the deviatoric and volumetric invariants of the plastic strain rate, respectively. Both components are assumed to follow Perzyna's overstress model of viscoplasticity [34]:

$$\begin{cases} \dot{\varepsilon}_q^{\mathrm{pl}} = \dot{\varepsilon}_{\mathrm{ref}} \left\langle \dfrac{q - y_q}{\sigma_{\mathrm{ref}}} \right\rangle^m \\ \dot{\varepsilon}_v^{\mathrm{pl}} = \dot{\varepsilon}_{\mathrm{ref}} \left\langle \dfrac{p' - y_{p'}}{\sigma_{\mathrm{ref}}} \right\rangle^m \end{cases} \tag{5}$$

where $\dot{\varepsilon}_{\mathrm{ref}}$ is a reference strain rate and m is the exponent in the power law stress–strain relationship. q and p' denote the equivalent deviatoric stress and the volumetric mean effective stress, respectively. $\langle \bullet \rangle$ represents the Macaulay brackets, such that

$$\langle \phi(p', q) \rangle = \begin{cases} \phi(p', q), & \text{if } \phi(p', q) \geq 0 \\ 0, & \text{if } \phi(p', q) < 0 \end{cases} \tag{6}$$

where $\phi(p', q)$ denotes the overstress function, which in our model is chemically dependent through the deviatoric and normal components of the yield stress, y_q and $y_{p'}$, respectively.

It is supported by laboratory evidence that the yield limit of carbonate rocks is affected by the reaction progress of mineral mass removal [10, 11]. Chemical reactions occur at local scale while the yield limit of a rock is a continuum-scale quantity. The concept of representative elementary volume (REV) is hence adopted to provide a bridge between the two scales. Here we consider a specific REV that satisfies the following conditions: (1) both the chemical and mechanical properties of the rock under investigation can be attributed to; (2) the size of the REV is larger than the characteristic length-scale of the chemical process considering diffusive transport; (3) the REV includes the presence of sufficient numbers of grains, pores, voids, and interactions between grains; (4) the REV can render the encapsulated material volume qualified as a continuum element in the process zone around the tip of the propagating crack.

The effect of chemical mass removal on the irreversible component of the rock mechanical behavior is expressed through a REV-averaged variable, ξ^{REV}, defined as

$$\xi^{\mathrm{REV}} = \int_0^t (1 + \eta\hat{\varepsilon})\dot{\xi}^{\mathrm{loc}} \mathrm{d}\tau \tag{7}$$

where $\hat{\varepsilon}$ denotes a strain invariant representing the local mechanical damage and η the coefficient of microcracking enhancement on the chemical process which is linked to the specific surface area of the pre-existing voids per unit volume in the matrix [26]. ξ^{REV} is hence interpreted as the time integration of the mass removal within the REV considering an enhancement on the local mass removal rate $\dot{\xi}^{\mathrm{loc}}$ by a mechanical variable representing the effect of microcracking. This REV-scale variable is bounded by $\xi^{\mathrm{REV}} \in [0, 1]$, where the lower limit denotes the pristine carbonate rock without any chemical dissolution while the upper limit corresponds to when all the dissolvable mineral mass is removed from the solid matrix.

Inside the REV, when irreversible deformation or damage is produced, new micro-crack walls are generated, increasing the total Specific Surface Area (SSA) of the solid–fluid interface per unit volume. Thereby, the total amount of mass removal by mineral dissolution is enhanced, assuming that the dissolution rate is proportional to the total SSA per unit volume of the REV. As a result, the stressed rock undergoing chemical erosion gets weakened, where local damage as well as the irreversible portion of deformation are in turn enhanced. A two-way chemo-mechanical coupling mechanism is therefore formed underlying the post-yield regime rock behavior. The yield limit, found to be dependent on the chemical progress, is here modeled as a function of ξ^{REV}. The following expression is adopted for describing the effect of chemical degradation on the yield limits:

$$y_{p',q} = Y_{p',q}\left(1 - \beta_{p',q}\xi^{\mathrm{REV}}\right) \tag{8}$$

where $Y_{p',q}$ denotes the normal or deviatoric component of the reference yield stress without any chemical dissolution. $\beta_{p',q}$ denotes the constant coefficients representing the effect of mass removal on the respective components of the yield limit.

Assuming an associated flow rule, the plastic strain rate in the form of second-order tensor is expressed as

$$\dot{\varepsilon}_{ij}^{pl} = \dot{\lambda}\partial f / \partial\sigma_{ij} \tag{9}$$

where f is the yield function and $\partial f / \partial\sigma_{ij}$ denotes the yield locus gradient giving the mode of plastic strain rate. Substituting Eqs. (4–8) into Eq. (9) we obtain the irreversible portion of the strain rate. Here the effect of chemical degradation is enabled through the scalar multiplier $\dot{\lambda}$, and the consideration of chemical reactions possibly changing the direction of the viscoplastic flow is out of the scope of this study.

2.2 Acid delivery coupled to damage evolution around the crack tip

We consider a macroscopic fracture undergoing subcritical growth in an above-described carbonate rock being affected by the chemical dissolution described by Eq. (1). How this single fracture would extend depends on the stress conditions as well as the chemical environment it is subject to. In the vicinity of the crack tip, local chemical environment for the rock material is not static but evolving due to the elevated damage associated with severe stressing around the tip, opening microcracks and affecting the delivery of acidic agents. Meanwhile, the acid delivery affects the local chemical dissolution as its reaction rate is dependent on the local concentration of the hydrogen. With an enhanced chemical mass removal, the rock material in the vicinity of the crack tip goes through further degradation. Therefore, acid transport through the aqueous phase and damage evolution in the solid matrix are coupled in a two-way manner.

2.2.1 Process zone around the tip of a subcritical crack

A process zone around the tip of a single fracture is illustrated in Fig. 1, where a blunt tip is considered to avoid

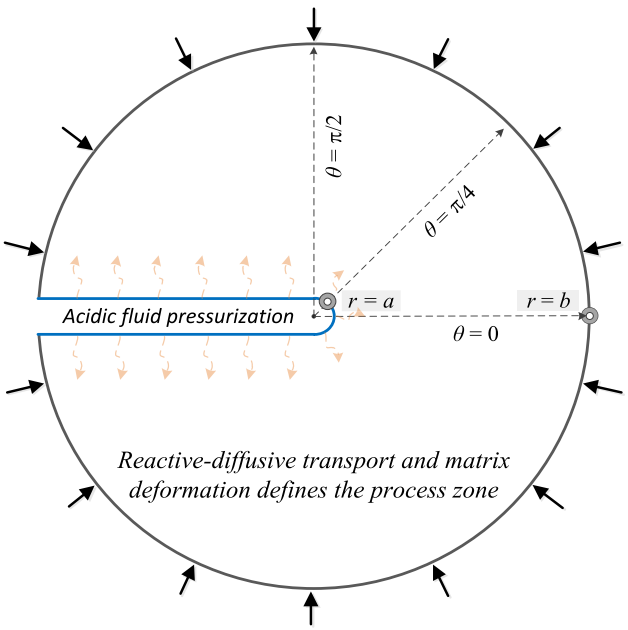

Fig. 1 Acid-assisted hydro-fracturing model of a single fracture in the presence of hydrogen invasion. The crack surface is subject to constant hydraulic pressure and acid exposure, and the exterior boundary is constrained by overburden pressure

the singularity problem associated with a sharp tip. The geometry of the fracture is defined as follows. The two fracture surfaces are parallel to each other with an opening of $2a$; at the fracture tip the curvature from $\theta = -\pi/2$ to $\theta = \pi/2$ is constant, $x = 1/a$ (see Fig. 1). To simulate acid-assisted fluid pressurization, a long-lasting acidic solution with a constant hydrogen concentration ($\mathrm{pH_{in}} = 5.3$) is pressurized inside the fracture opening, posing a uniformly distributed fluid pressure p_{in} on the crack surfaces and the tip. On the exterior boundary ($r = \mathrm{b}$), a uniformly distributed confining pressure p_{ex} representing the overburden is considered. An extremely low permeability carbonate is considered, assuming negligible evolution of the rock porosity with the chemical process. The chemically induced degradation of the rock is manifested in both the elastic and plastic domains of rock behavior. Inside the process zone, both the elastic modulus and yield limit are affected by the process of damage-enhanced mass removal. The chemical boundary condition on the exterior of the process zone is assumed as unconstrained. For the initial conditions, a neutral pH environment is applied to the entire process zone which is selected as the reference hydrogen concentration.

2.2.2 The role of damage in reactive transport within the process zone

Transport of the dissolved mineral mass is here described by a reactive–diffusion equation with a nonlinear source term representing the rate of mass flux generated from the damage-enhanced chemical dissolution processes. Advective transport is assumed negligible. On the chemical part, dissolution occurs when a reactive species (hydrogen, H^+) attacks the soluble matter ($CaCO_3$) which consumes the reactive agent. The reaction/dissolution will stop when the soluble mass or the reactive agent is exhausted, whichever occurs earlier. In this contribution we chose to consider the former case in an open system scenario, which allows flux of ions entering or exiting the system from/to the environment, formulating boundary value problems (BVPs) well constrained from both the mechanical and chemical fields. One prominent motivation is that emergent phenomena or self-organized spatio-temporal patterns [23, 24] often occur resulting from coupled multiphysics reaction–diffusion feedback processes, which operate away from thermodynamic equilibrium relaxing the constraints of a closed system. Our viscoplasticity based model hence simplifies the chemical damage model of Borja et al. [7] inspired by the transition state theory while capturing the ductilization effect induced by the diffusion of surrounding chemical environment, supported by laboratory evidence shown in the post-peak regimes of calcarenites tests [10, 11].

Following the kinetics of calcite dissolution given by Sjöberg and Rickard [44], the rate of the dissolution of $CaCO_3$ is assumed as a power law function of the local hydrogen concentration $C_{\mathrm{H^+}}$, which leads to the reactive-transport process of Ca^{2+} being coupled to the irreversible damage of the solid matrix as well as the delivery of hydrogen:

$$\partial_t x_{\mathrm{Ca^{2+}}} = D_{\mathrm{Ca^{2+}}} \nabla^2 x_{\mathrm{Ca^{2+}}} + \beta_{\mathrm{H^+}} (1 + \eta \hat{\varepsilon}) (C_{\mathrm{H^+}})^{k'} \tag{10}$$

where $x_{\mathrm{Ca^{2+}}}$ denotes the molar fraction of calcium in the fluid phase within the process zone, $D_{\mathrm{Ca^{2+}}}$ denoting the diffusivity of calcium, assumed as constant in the process zone. $\beta_{\mathrm{H^+}}$ denotes a lumped constant representing a combined effect of local acidity and damage enhancement on the mass dissolution rate. The exponent k' is usually assumed as constant with a value between 0.5 and 1.0, and $k' = 0.9$ is adopted in the present study [43]. The evolution of acidity distribution over time is controlled by

$$\partial_t C_{\mathrm{H^+}} = D_{\mathrm{H^+}} \nabla^2 C_{\mathrm{H^+}} - \gamma_{\mathrm{CH}} \dot{\xi}^{\mathrm{REV}} \tag{11}$$

where $D_{\mathrm{H^+}}$ denotes the diffusivity of hydrogen and γ_{CH} is a proportionality constant of the concentration change rate of hydrogen due to consumption over the mass transfer rate of calcium production in the REV. To this end, the reactive–diffusion of calcium, the spreading of acidity, the chemical dissolution occurring at the solid–fluid interfacial areas, and the matrix yielding as well as the dissipative micro-cracking process are fully coupled.

3 Computational method

3.1 Finite element implementation of the proposed reactive-chemo-mechanical framework

An open-source finite element simulator, MOOSE [17, 35, 36], is employed as the numerical platform to implement Eqs. (2–11) for investigating the problem of subcritical crack propagation in a carbonate considering chemical degradation and the associated reactive transport of solute as well as damage-dependent acid delivery in the process zone. The involved complex process is described by three modules, representing the chemically affected mechanical behavior, the progress of mineral dissolution, and the damage-dependent transport processes. The three modules are tightly connected interactively via the involved parameters enclosing the state information at each time step for each feeding back or forward. The family of finite element shape functions for all unknown variables to

be solved in PDEs, including displacement (u_x, u_z, u_z) and solute concentration (C_{H^+}, $x_{Ca^{2+}}$), is linear Lagrange with the first order form. Newton–Raphson algorithm is adopted to calculate the increments of the elasto-visco-plastic variables at each timestep. ConstantDT timestepper is used which initially simply takes a constant time step size throughout the analysis unless the solver fails to converge on an iteration. In what followed, the time step size is repeatedly cut back until a successful solution is obtained.

To describe the system response under loading, the elastic and plastic regimes of rock behavior are influenced by the local dissolution rate ξ^{loc} and a REV-scale mass removal ξ^{REV} taking into account the irreversible micro-cracking and path-dependence in time. Meanwhile, the progressive degradation of rock strength leads to further damage and the newly generated micro-fracturation acts as an addition to the SSA per unit volume accelerating the overall chemical mass removal rate. This internal mass exchange process serves as the source or sink terms in the reaction–diffusion equations of ion transport, and hence the transport process is coupled to the irreversible deformation of the rock. In MOOSE implementation, a plasticity check at each node is incorporated for each Newton–Raphson iteration to determine if the material point enters the plasticity regime. In the elastic regime, for example the area near the exterior, only the elasticity tensor is updated with an updated amount of mass removal from the reaction-transport processes at each time step. Once plasticity is reached, i.e., in the vicinity of the fracture tip where stress concentrates, the incremental plastic flow, the flow tensor, the deviatoric and volumetric components of the yield stress as well as the damage proxy get updated at each iteration.

The above-discussed physico-chemical processes originating from the micro-scale are linked to a continuum-scale description of rock behavior via the selected REV. Details on how kernels and auxiliary kernels are established for the coupled reactive-chemo-mechanical model can be found in the Appendix of the reference [46]. For the investigation of acid-assisted subcritical crack propagation, all the involved physico-mechano-chemical variables and parameters are normalized for the numerical implementation. The normalization rules for a conversion of the system description into a dimensionless group are outlined as

$$x^{\star} = \frac{x}{L_{\mathrm{ref}}}, \quad \sigma_{ij}^{\star} = \frac{\sigma_{ij}}{\sigma_{\mathrm{ref}}}, \quad C^{\star} = \frac{C}{C_{\mathrm{ref}}}, \quad t^{\star} = \frac{t}{t_{\mathrm{ref}}} \tag{12}$$

where L_{ref}, σ_{ref}, C_{ref}, and t_{ref} denote the reference values for displacement, stress, concentration and time, respectively. In the current study, the initial radius of the cavity is chosen to be the reference length L_{ref}. The selection of t_{ref} is made based on $t_{\mathrm{ref}} = \frac{L_{\mathrm{ref}}^2}{D_{\mathrm{H}^+,\mathrm{ref}}}$, where $D_{\mathrm{H}^+,\mathrm{ref}}$ denotes a reference value for the diffusivity of hydrogen (Hu and Hueckel 2019). C_{ref} here represents the hydrogen concentration in a neutral condition where no dissolution occurs. The reference for the stress components is commonly the initial value of rock cohesion. For all the numerical investigations in this study, mesh refinement and a small enough time-step are incorporated to ensure the accuracy of our results from our numerical experiments. Under sufficiently large fluid pressurization, slip-line field is expected to develop from the assumed round-tip of a blunt fracture (as illustrated in Fig. 1) following the trace of logarithmic spirals [31]. In what follows, we first benchmark the implemented code with the analytical solution of the slip-line field for an internally pressurized thick-walled cylinder.

3.2 Benchmarking against Johnson's analytical solution of an internally pressurized cylinder

Before proceeding to the numerical investigation of subcritical cracking, this section presents benchmark tests of the implemented code against the analytical solution [31] of the slip-line field around an internally pressurized thick-walled cylinder, as depicted in Fig. 2. Two-dimensional quadrilateral mesh (3107 elements in total) is used, and the mesh size is progressively smaller as getting closer to the cavity wall. Ideal rigid plasticity is assumed for the material under consideration. No chemical dissolution or

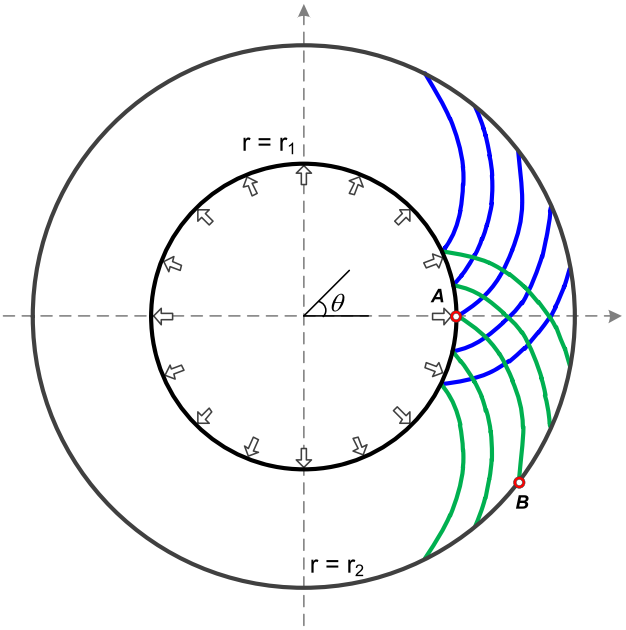

Fig. 2 Slip line field solution for the expansion of a circular hole in an ideal rigid-plastic medium. Radial pressure is applied at $r = r_1$, traction-free condition assumed at $r = r_2$. With the assumption of von Mises material, the α slip lines (in blue) and β slip lines (in green) are orthogonal at crossing points (color figure online)

internal erosion is considered here. The pressure variation on slip lines is described by Hencky's equations. The hydrostatic pressure $\overline{\sigma}$ varies with the angle φ along the slip line in a linear relationship with the yield stress k:

$$\overline{\sigma} - 2k\varphi = \text{C1 along } \alpha \text{ line} \tag{13a}$$

$$\overline{\sigma} + 2k\varphi = \text{C2 along } \beta \text{ line} \tag{13b}$$

The boundary conditions are uniformly distributed radial pressure applied on the interior of the cylinder and the exterior free of traction. Plane strain conditions are assumed. The maximum and minimum principal stresses in this case are $\sigma_1 = \sigma_\theta$ and $\sigma_3 = \sigma_r$, corresponding to $\frac{1}{2}(\sigma_\theta - \sigma_r) = k$ for von Mises materials (i.e., yielding upon the second invariant of deviatoric stress reaches a critical value) according to the Mohr's circle criterion. A slip line growing from an arbitrary point of the interior, for instance, AB in a logarithmic form, takes the mathematical description $r = r_1 e^{\varphi}$. At the traction-free point B, $\sigma_{\mathrm{r}} = 0$, $\sigma_\theta = 2k$ which can be derived from the yield criterion, and $\varphi_B = \ln\frac{r_2}{r_1}$. The value of C1 along the α line can be obtained via Hencky's equations:

$$\mathrm{C1}_B = \frac{1}{2}(\sigma_\theta + \sigma_{\mathrm{r}}) - 2k\ln\frac{r}{r_1} = k - 2k\ln\frac{r_2}{r_1} \tag{14}$$

With the assumed ideal rigid plasticity, the radial and circumferential stress components at any point can be expressed as

$$\sigma_{\mathrm{r}} = -2k\ln\left(\frac{r_2}{r}\right) \tag{15a}$$

$$\sigma_\theta = -2k\ln\left(\frac{r_2}{r}\right) + 2k \tag{15b}$$

The von Mises material under consideration is assigned with a yield stress $k = 20\,\mathrm{MPa}$ over the entire region. Rigid plasticity is modeled by taking a sufficiently large exponent (here $m = 20$ is adopted) in the power law relationship [25]. A comparison of the distribution of the radial, circumferential and shear stress components along the radius computed from the analytical solution (by marks) and the numerical implementation (by solid curves), respectively, is illustrated in Fig. 3. Zero difference shows between the numerical and analytical solutions of the radial distribution of the shear stress component. The numerical results of the distribution of σ_{rr} and $\sigma_{\theta\theta}$ along the radius show R^2 values of 0.9999 and 0.9998, respectively, in comparison with the analytical solution. Benchmarking against the classical thick-walled cylinder problem demonstrates the capability of the implemented numerical code as a robust simulator for processes involving plastic deformation.

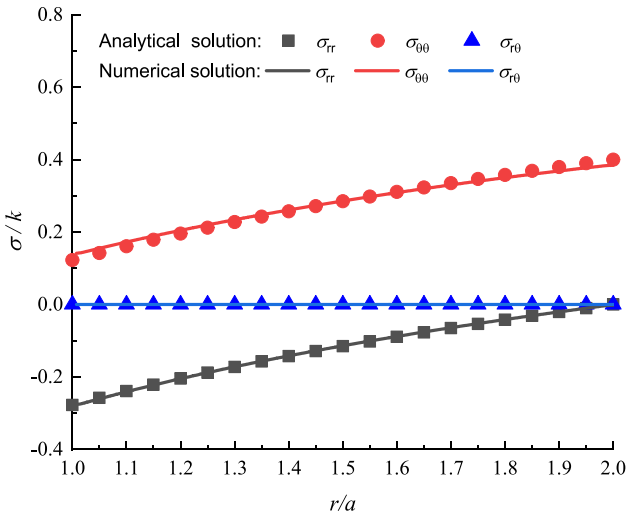

Fig. 3 Distribution of stress components along the cylinder radius. This benchmarking against Johnson's analytical solution demonstrates the simulator as a robust numerical platform for plasticity computations

4 Simulation results

In what follows, we present our simulation results on subcritical growth of a single fracture subject to fluid pressurization and a chemically reactive environment as illustrated in Fig. 1 (98,876 elements in total are used with mesh size made smaller gradually as is closer to the crack tip surface). Plane strain conditions and von Mises yield criterion are assumed. Acidic agents are diffusing into the process zone around the tip point in the carbonate rock with a constant source concentration at pH = 5.3, from the crack surfaces and the tip, and a neutral pH environment is assumed as the initial condition for the entire material. The mechanical boundary conditions are a uniform fluid pressure $p_{\mathrm{in}} = 0.4\,\mathrm{MPa}$ acting on both the crack surfaces and the tip and a confining pressure p_{ex} here set as vanishing on the exterior of the process zone. A mild value of fluid pressurization is used to emphasize on the chemically induced yielding enabled by the diffusion of acidic agents. The basic mechanical properties of the carbonate rock used in this study include the initial Young's modulus $E_0 = 20\,\mathrm{GPa}$, Poisson's ratio $\upsilon = 0.25$ and the initial rock cohesion $c_0 = 10\,\mathrm{MPa}$. The size of the process zone is assumed extending to the radius $b = 10 * a$, where a is the radius of the round-tip of the blunt crack, here set as $a = 1.5\,\mathrm{mm}$. The diffusivity of hydrogen takes the value $D_{\mathrm{H}^+} = 3.6 \times 10^{-5}\,\mathrm{cm}^2/\mathrm{s}$ after Fredd and Fogler [14]. The other input parameters for the coupled reactive-chemo-mechanical system underlying the crack-tip process zone include $\beta_p = 0$, $\beta_q = 1$, $\eta = 2 \times 10^4$ [26, 46], $k' = 0.9$, $\beta_{\mathrm{H}^+} = 2.5 \times 10^{-3}$ [11], if not specified or subject to a parametric study.

4.1 Evolution of chemical mass removal and the stress field around the crack tip

For the acid-assisted subcritical crack propagation problem under investigation (see Fig. 1), the stress field involved is no longer axisymmetric, but symmetric with respect to the crack propagation direction ($\theta = 0$). The distribution of the deviatoric stress invariant along the radius at three directions ($\theta = 0, \pi/4, \pi/2$) upon an exposure of 900 h is illustrated in Fig. 4. It is shown that along the direction perpendicular to the crack propagation direction (i.e., at $\theta = \pi/2$) the deviatoric stress is relatively mild, with the value decreasing from the crack tip toward the exterior. At the direction $\theta = \pi/4$, the deviatoric stress is significantly higher near the tip with the maximum value reaching $0.8C_0$ and the distribution along the radius follows still a monotonically decreasing trend. The radial distribution of the deviatoric stress at the crack propagation direction ($\theta = 0$) is, however, nonmonotonic, with the location of the maximum value slightly ahead of the tip (around $1.1a$). This strong nonlinearity arises from the severe stressing at the crack tip area interacting with the damage-affected chemical processes, which is also shown in the inset of Fig. 1 showing the contour representation of the normalized deviatoric stress in the vicinity of the crack tip.

The stress drop between $r = a$ and $r = 1.1a$ also suggests a dramatic effect of chemical degradation that is commonly observed for stressed materials exposed to a reactive environment for a sufficient long duration, for example in the experimental observations on calcarenite specimens [11]. The yield limit of a dissolvable rock drops as a result of chemical degradation. Figure 5 further shows the evolution of the radial distribution of the deviatoric stress along the crack propagation direction at an early (up to several days) and later (more than 1 month) stages, with Fig. 5a depicting the deviatoric stress distribution for $t = 10, 50, 100$ h of exposure and Fig. 5b for $t = 300, 600, 900$ h of exposure. The non-monotonicity in the radial distribution starts to appear after 100 h, and becomes more pronounced in the later stage as shown in Fig. 5b due to an accumulated effect of chemical degradation concentrating in front of the crack tip. Quantitatively, the normalized deviatoric stress invariant (q/c_0) at the tip reaches 0.936, 0.813, and 0.544, after $t = 300, 600, 900$ h, respectively, which corresponds to 0.064, 0.187, and 0.456 of total mass removal (see Fig. 6) at the tip point.

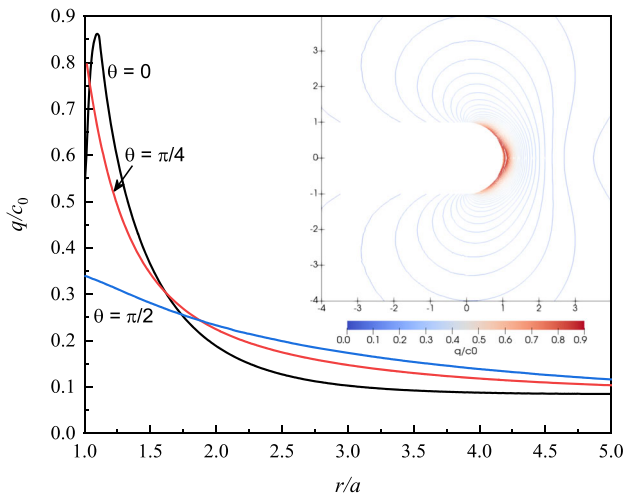

Fig. 4 Distribution of deviatoric stress normalized by the initial cohesion along radius at three trajectories ($\theta = 0$, $\pi/4$, $\pi/2$) at a timestep with 900 h of exposure

Figure 6 depicts the evolution of the accumulated mass removal with two representative points on the round-tip of the crack at $\theta = 0$ and $\pi/2$, respectively. At $\theta = \pi/2$, the time evolution up to 1000 h is close to a linear trend as no significant damage enhancement involved. In comparison, a clear acceleration in the time evolution of the mass removal ξ^{REV} is observed at $\theta = 0$, resulting in the value 3.3 times of the counterpart at $\theta = \pi/2$ at the end of 900 h exposure. At the cack tip point along the crack propagation direction where stress concentrates, the effect of chemical softening is enhanced as a result of intensified damage evolution. Continuously increasing SSA per unit volume due to damage serves as additional solid–fluid interfaces providing extra locations for mineral dissolution to occur, resulting in a higher dissolution rate and hence an enhanced regional chemical degradation, as evidenced in Fig. 4. The distribution of deviatoric stress and deviatoric strain fields around the crack tip at $t = 900$ h, is shown in the insets of Figs. 4 and 6, respectively. The contours show a general agreement with the stress and deformation concentration in the vicinity of the crack approximated by the classical linear elastic fracture mechanics (LEFM) for plane-strain Mode I fracture scenarios [2]. Plasticity is very much confined in the near-tip area, within the region of a radius $1.1a$ at $t = 900$ h (see Fig. 5), as a result of mild fluid pressurization imposed on the crack opening allowing for a chemically enabled yielding that extends from the blunt-tip.

Figure 7 depicts a comparison between the evolution of distribution of acidity along the radius in the two directions ($\theta = 0, \pi/2$). At an early stage (e.g. within several days) of acid exposure, as shown in Fig. 7a, the pH value of the domain chemical environment represented by the radial distribution along both directions increases at a fast rate, indicating a diffusion-dominant transport of hydrogen. In contrast, upon a longer period of exposure, e.g. approximately 1 month as shown in Fig. 7b, the acidity distribution in the process zone becomes stabilized, close to a steady-state where the acidity over the entire process zone

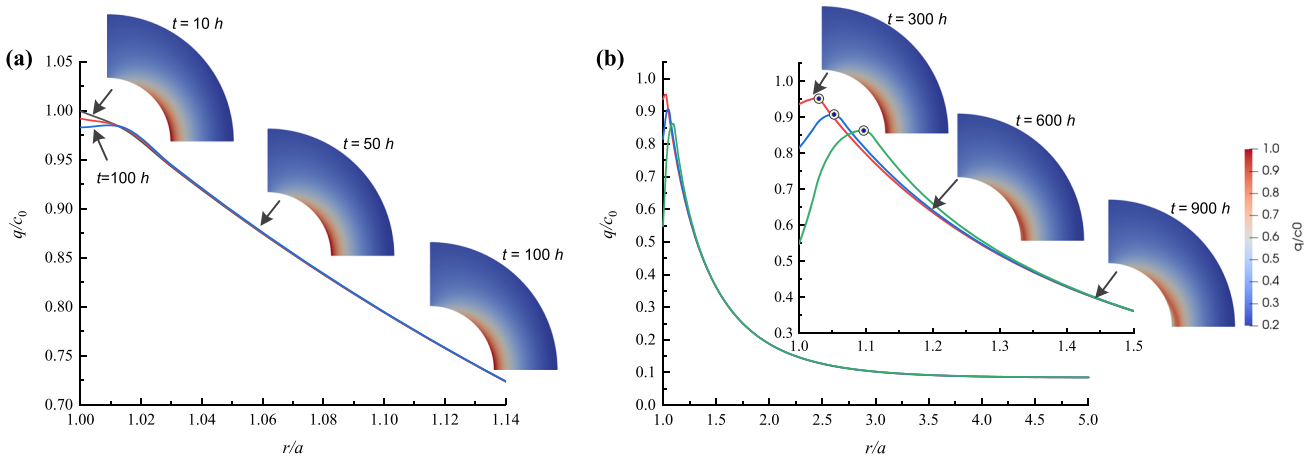

Fig. 5 Evolution of the distribution of deviatoric stress normalized by the initial cohesion along the radius at propagation direction (θ = 0), upon **a** 10, 50 and 100 and **b** 300, 600, and 900 h of exposure

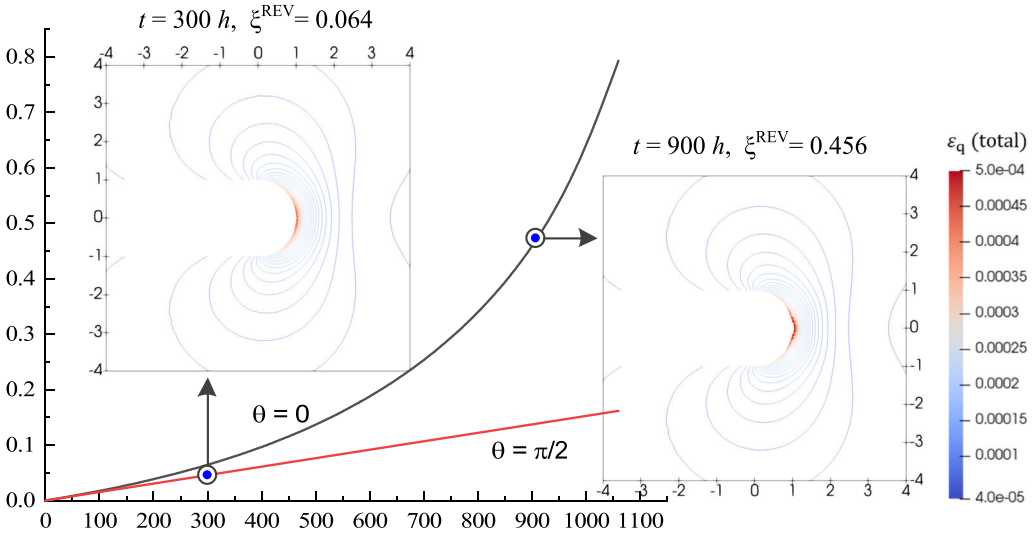

Fig. 6 Evolution of the accumulated mass removal at crack tip point during a long-term acid pressurization. The contours of the deviatoric strain (total strain) suggest an emergence of localized damage near the tip region, accelerating mineral dissolution, under the combined action of acidizing and pressurization

is equal to the acidity inside the crack opening. Compared to the axisymmetric scenarios, for instance the cavity expansion case [46], the evolution of the acid distribution exhibits a directional spreading in the process zone. Specifically, along the direction perpendicular to crack extension (at $\theta = \pi/2$, represented by the dashed curve) the acid front propagates faster than the counterpart along $\theta = 0$ (the direction of crack extension, represented by the dashed curve), which is more pronounced in the early stage. This is due to the fact that the acid consumption in front of the crack tip along the extension direction is significantly higher, as indicated in the mass removal development in Fig. 6.

We further explore the time evolution of the accumulated mass removal in a selected domain surrounding the crack tip. We select a round region of a radius equal to $2a$ at the crack tip as shown in Fig. 8a and plot the evolution of the integrated REV-scale mass removal in this selected domain under varying acid intensity in Fig. 8b. With a higher chemical intensity imposed at the crack tip, the integration of the mass removal ξ^{REV} over the domain grows faster, as a result of a higher concentration of hydrogen diffusing into the carbonate rock matrix causing an elevated mineral mass removal. The time evolution of the accumulated mass removal under the different chemical conditions is nearly linear as observed from Fig. 8b. This is because the damage-enhancement zone where an accelerated mass removal occurs takes only a small portion of the selected region, which results in no evident acceleration in the domain integration of the total mass removal. With an

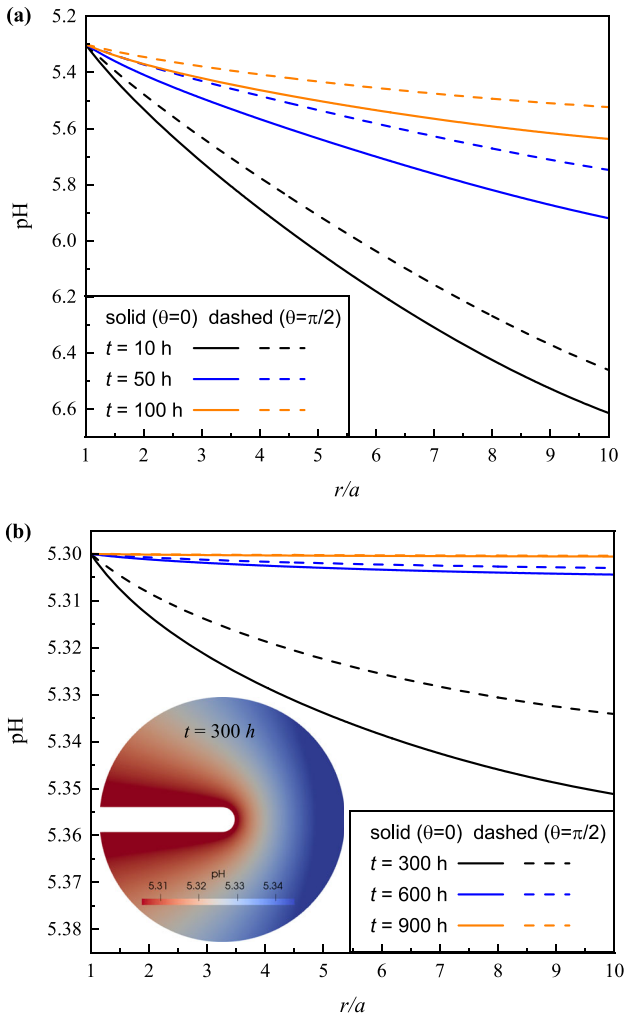

Fig. 7 Evolution of the distribution of acidity (represented by pH values) along radius at propagation direction (θ = 0, solid line) and perpendicular trajectory (θ = π/2, dashed line), upon 300, 600 and 900 h of exposure of the combined action of acidizing and pressurization

imposed $pH_a = 5.3$, the mass removal over the domain is approximately 4.25 times of the counterpart with $pH_a = 6.0$ at any given time, as Fig. 8b shows. Another influencing factor commonly considered is the microcracking enhancement on the chemical dissolution, namely the parameter η, which plays an insignificant role in the evolution of the accumulated mass removal integrated in the selected domain (not shown here), also due to the very small plasticity zone developed in front of the crack tip [46].

4.2 The role of imposed chemical environment and micro-cracking in front of the blunt-tip

Subcritical crack propagation can be induced in carbonate rocks under constant fluid pressurization containing acidic agents [26, 27]. Mass removal by chemical dissolution causes degradation of rock properties, alteration in acid delivery as well as a redistribution of the stress and strain fields in the near-crack tip area. Classically, subcritical propagation of a crack is described by the correlation between the logarithmic of crack propagation velocity and the Stress Intensity Factor (SIF). Before examining such relationships, we first plot the time evolution of the displacement of the tip point ($r = a, \theta = 0$) that represents crack propagation under various chemical environments, as shown in Fig. 9a. For the case of $pH_a = 6.0$, the displacement of the crack tip point shows an insignificant development, especially when compared with the cases of $pH_a = 5.6$ and $pH_a = 5.3$. With a lower value of pH_a representing a higher intensity of acid exposure, the crack propagates much faster due to (1) damage-enhanced mineral mass removal and hence an enhanced chemical degradation, and (2) improved acid delivery into the process zone enabled by damage evolution. For example, when exposed to a chemical environment of $pH_a = 5.3$, the crack propagates further into the stressed rock by more than one magnitude than with an environment of $pH_a = 5.6$ after 1000 h. The combination of the above-mentioned two effects is also responsible for the prominent nonlinearity observed in the propagation of crack versus time under a relatively low pH environment (e.g. here $pH_a = 5.3$).

The effect of the microcracking enhancement coefficient, η, on the crack propagation over time is illustrated in Fig. 9b. For the case of $\eta = 0$, representing a one-way coupling (i.e., the process of microcracking does not pose an effect on the progress of chemical mass removal), the displacement of the crack tip displays a mild development. For the case $\eta = 1 \times 10^4$, as the reaction progresses, the crack propagation shows an exponential development over time. When micro-fracturation coefficient is doubled, i.e. $\eta = 2 \times 10^4$ (meaning e.g. the material is more susceptible to microcracking under the action of stressing), the crack propagation demonstrates a substantial increase in terms of displacement and its rate. This acceleration results from the mutually promoting mechanism of chemical mass removal and material degradation, i.e., a two-way feedback loop pronounces in such an evolving complex system.

Originating from classical fracture mechanics, the SIF for crack propagation that relates to the energy release rate during propagation (i.e. opening of crack surface area) represents an energetic parameter characterizing the fracture toughness of the material in the near-crack tip area. The *J*-line integral is often adopted to compute the strain energy release rate along a closed contour, given below:

$$J = \int \left(W \mathrm{d}x_2 - T_i \frac{\partial u_i}{\partial x_1} \mathrm{d}s \right) \tag{15}$$

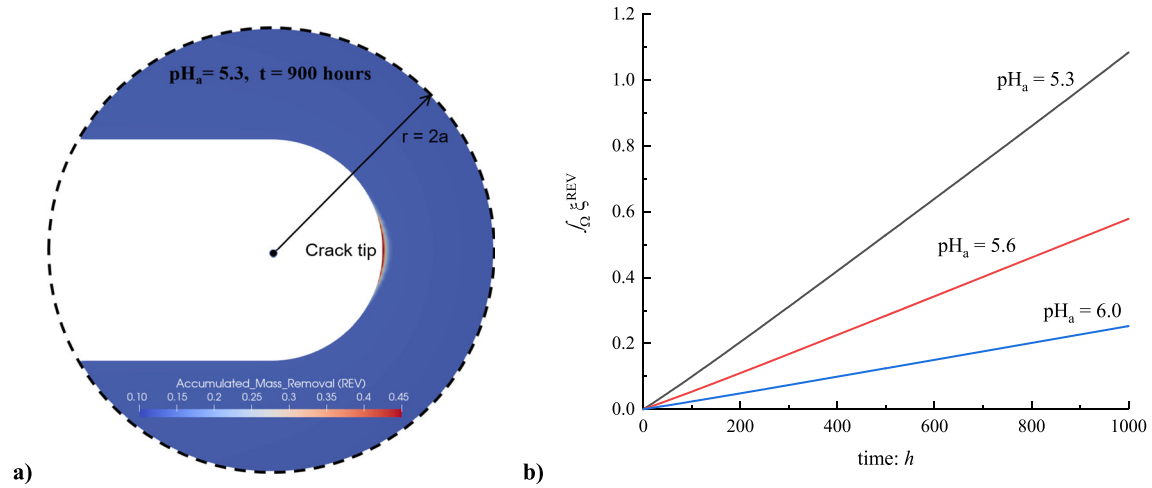

Fig. 8 Time evolution of the integrated REV-scale mass removal in a selected domain: **a** illustration of the selected domain, here a round region with $r = 2a$; **b** with a variety of acid intensity imposed at the cavity wall, for $\mathrm{pH}_a = 5.3$, $\mathrm{pH}_a = 5.6$, $\mathrm{pH}_a = 6.0$, respectively

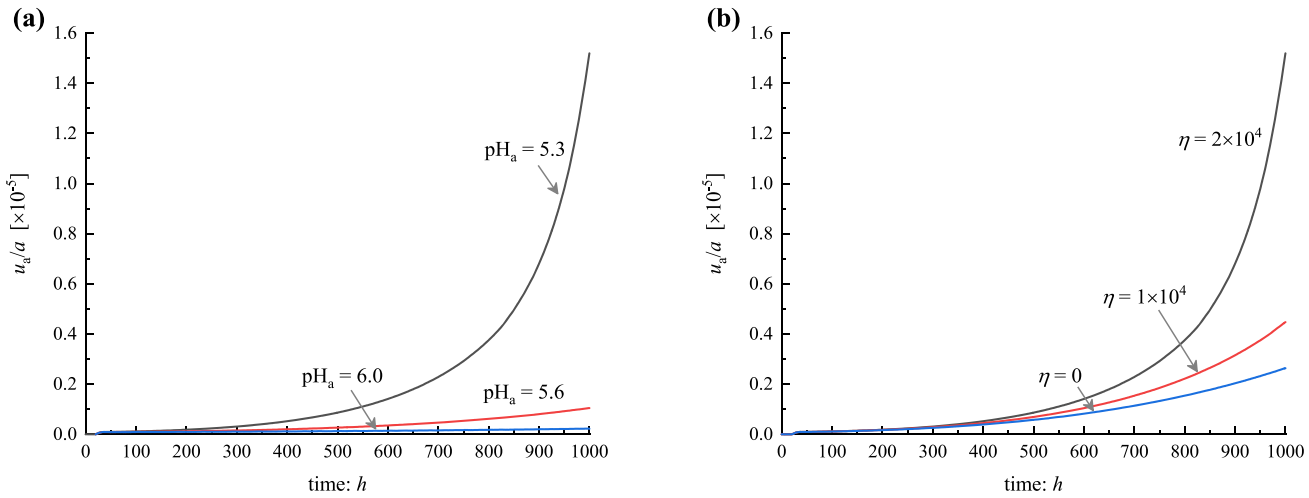

Fig. 9 Time evolution of the crack propagation represented by the normalized movement of crack tip point: **a** with a variety of acid intensity imposed at cavity wall, for $\mathrm{pH}_a = 5.3$, $\mathrm{pH}_a = 5.6$, $\mathrm{pH}_a = 6.0$, respectively; and **b** with microcracking coupling coefficient $\eta = 0, 1 \times 10^4, 2 \times 10^4$, respectively

where x_1 and x_2 represent the coordinate directions parallel and perpendicular to the crack propagation direction, i.e., $\theta = 0$ and $\theta = \pi/2$, respectively. W is the strain energy density, expressed as $W = \int \sigma_{ij} \mathrm{d}\varepsilon_{ij}$. T_i is the surface traction pointing outward and normal to a contour path and ds is the arc length along the contour path. u_i, σ_{ij} and ε_{ij} denote displacement vector, stress tensor and total strain tensor, respectively.

For Mode I (tensile) loading, as in the current case of fluid pressurization from the crack opening, the SIF (K_1) can be computed from the J-integral via the relation $J = \frac{1-\nu^2}{E} K_1^2$. By considering a blunt-tip crack, the singularity problem that commonly associates with a sharp tip is alleviated and the contour along the blunt-tip as the crack extends is chosen as the integration path for computing the J-integral. It is found that K_1 of a single fracture under a combined action of fluid pressurization and acid infiltration from the crack opening (as described in Fig. 1) increases as the time progresses. The effect of chemical boundary conditions on the time evolution of K_1 is illustrated in Fig. 10a. With a mild acidity applied on the boundary as $\mathrm{pH}_a = 6.0$, the SIF increases insignificantly as the crack extends over time, i.e., the redistribution of stress and deformation in the vicinity of the crack tip can just offset the effect of chemical softening on reducing the fracture toughness. For a higher acidity, as shown in the case of $\mathrm{pH}_a = 5.3$, the SIF increases faster with respect to the reaction time, and shows an overall exponential development. As discussed earlier, a higher hydrogen concentration induces a more intense degradation of the mechanical properties of the material around the tip in both the elastic

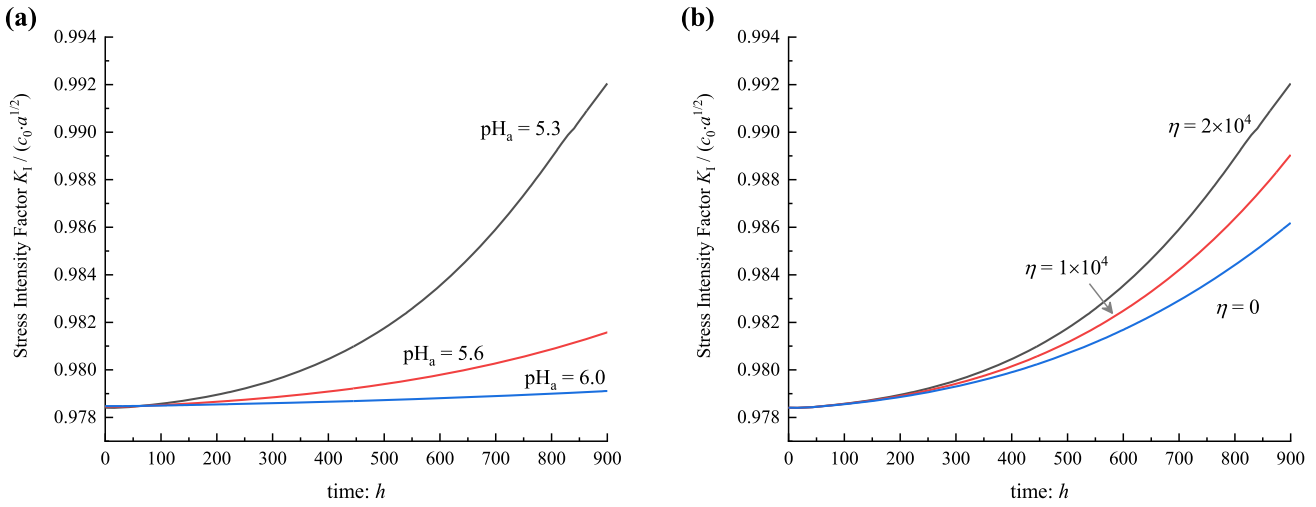

Fig. 10 Time evolution of the normalized stress intensity factor during progressive crack propagation: **a** with a variety of acid intensity imposed at cavity wall, for $pH_a = 5.3$, $pH_a = 5.6$, $pH_a = 6.0$, respectively; and **b** with microcracking coupling coefficient $\eta = 0, 1 \times 10^4, 2 \times 10^4$, respectively

and plastic regimes, which contributes to a reduction in the strain energy density of rock under the combined chemo-mechanical loading. Meanwhile, the stored elastic energy increases as the energy required to form new crack surfaces decreases due to the chemical softening on the near-tip material, based on energy conservation. The competition of these two mechanisms results in a higher level of fluid acidity and drives more overall strain energy stored in materials around the crack tip, as indicated by the tensile SIF K_1 (Fig. 10a) leading to a faster propagation of the crack tip (Fig. 9a). As for the effect of the microcracking enhancement, we observe that the calculated K_1 evolves exponentially as the crack tip propagates, for the one-way coupling case ($\eta = 0$, no micro-cracking enhancement), as shown in Fig. 10b. For a higher value of the coefficient η, K_1 accelerates faster as the crack tip propagates. This suggests that the more susceptible the rock is to microcracking under stress, the more overall strain energy is stored in the near-tip region as the crack extends under a combined action of pressurization and acid infiltration.

The evolution curve of crack tip velocity (in logarithmic scale) versus Mode I (tensile) stress intensity factor K_I is illustrated in Fig. 11. With K_I upon loading as the driving parameter, three regions of the development of crack propagation rate are identified. In the low propagation rate regime, the acceleration of the crack growth rate with respect to K_I goes through a smooth decrease, characterizing Region I as shown in Fig. 11. This corresponds to that at an early stage (a few days) the crack propagation in the carbonate rock is controlled by the rate of the reaction between the acidic agents that are diffusing into the rock matrix and the dissolvable minerals being removed from the matrix. It is hence hypothesized that the crack growth

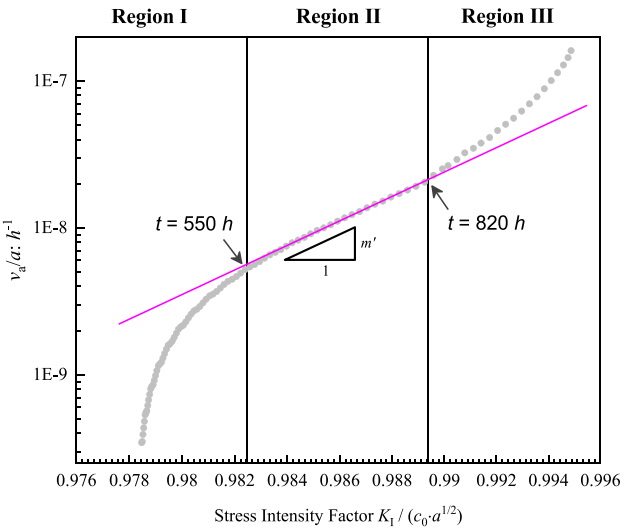

Fig. 11 Crack tip velocity (in logarithmic scale) versus Mode I (tensile) stress intensity factor (SIF) K_I at the crack tip. Three regions are observed during acid-assisted crack propagation and the second Region obeys a power law pattern

in Region I is mainly influenced by the environmental aspects, in particular the local hydrogen activity that controls the local mass removal rate $\dot{\xi}$. The role of environmental acidity on the evolution of the crack growth rate versus stress intensity factor K_I is illustrated in Fig. 12a. It is shown that a more acidic environment leads to an overall faster crack propagation for the same SIF. At the beginning of the process, the crack growth rate in the case of $pH_a = 5.3$ is higher than the weakest acid case (i.e. $pH_a = 6.0$) by approximately one order of magnitude. It is also observed in Fig. 12a that for the case of $pH_a = 5.3$ the acceleration of the crack propagation velocity is slightly higher than the

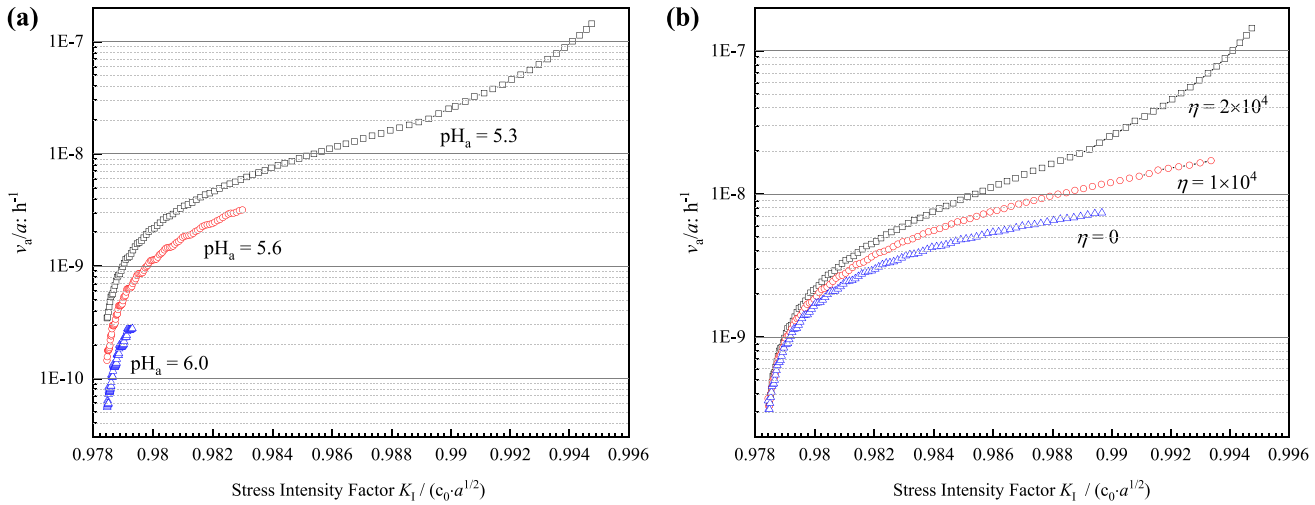

Fig. 12 Crack tip velocity (in logarithmic scale) versus Mode I (tensile) stress intensity factor (SIF) K_I at the crack tip: **a** with a variety of acid intensity imposed at cavity wall, for $pH_a = 5.3$, $pH_a = 5.6$, $pH_a = 6.0$, respectively; and **b** with microcracking coupling coefficient $\eta = 0, 1 \times 10^4, 2 \times 10^4$, respectively

other cases when the crack reaches the same fracture toughness in Region I.

As the process continues, the distribution of hydrogen concentration over the system is approaching a steady state and the pH value in the process zone gets stabilized indicating a nearly uniform distribution of the local reaction rate. The crack propagation hence enters Region II, as shown in Fig. 11, featuring an intermediate range of the crack propagation rate with a constant acceleration (in logarithmic scale) with respect to the stress intensity factor K_I. This constant acceleration is also the lowest among the three regions. The crack propagation slows down in Region II due to that the hydrogen delivery lags behind the propagating front of the stress concentration in the near-tip area and the reaction is hence slowed down. We hypothesize that in Region II microcracking develops in front of the crack tip to facilitate the acid delivery, preparing the crack propagation for entering Region III.

In Region III, the near-tip area is subject to a relatively uniform chemical environment with elevated acidity, and the crack propagation rate increases with a growing acceleration that roots in the micro-fracturation enhancement on the reaction. As the total mass removal is enhanced by severe stressing induced micro-cracking in the near-tip area, the crack tip propagates at a fast rate correlating with a higher stress intensity factor. Figure 12b shows a comparison between the crack propagation rate versus K_I with various micro-cracking enhancement coefficients. In Region I, the difference between the three curves is insignificant, supporting the hypothesis that the crack propagation during this stage is mainly reaction-controlled and the extent of micro-cracking is limited. In Region II, the acceleration in the propagation rate for an increasing micro-cracking enhancement coefficient shows a mild increment, especially compared with Region III. For the case of $\eta = 2 \times 10^4$, the crack propagation rate increases with a more dramatic acceleration compared to the case of $\eta = 1 \times 10^4$ in Region III, substantiating the proposition that micro-fracturation enhancement on the reaction is a controlling parameter. In other words, in this region the more susceptible the rock is to microcracking under stress, the more accelerated the crack grows (see Fig. 12b).

4.3 The effect of initial imperfections on the subcritical growth of a macroscopic crack

In what follows, we investigate the effect of material heterogeneity on the subcritical propagation of the pressurized macroscopic crack under acidizing. The heterogeneity is introduced to the system by imposing a randomly distributed local mass removal, i.e. within the range of [0, 0.05] on the entire process zone as the initial conditions, simulating an inhomogeneous distribution of mechanical properties. Specifically, the heterogeneity is assigned to the spatial distribution of the initial elasticity modulus and the initial yield limit of the rock according to the chemo-mechanical model adopted in this study (see Sect. 2.1). Due to the imposed inhomogeneity, a redistribution of the initial stress field in the process zone occurs at the first time step, acting as a small perturbation for the rock containing a macroscopic crack undergoing chemically enabled subcritical growth.

The time evolution of the distribution of accumulated mass removal along the radius at the crack propagation

direction is depicted in Fig. 13a. At the beginning of the process ($t = 10$ h), small fluctuations exhibit in the mass removal profile as a result of the imposed initial heterogeneity. The fluctuation in the distribution of the accumulated mass removal appears to be denser within the range of $1 < \frac{r}{a} < 2$ due to a necessary incorporation of mesh refinement in the near-tip region. As the reaction progresses, e.g. from $t = 300$ h to $t = 600$ h, we notice that the accumulated mass removal starts to undergo a dramatic development near the crack tip compared to the rest of the process zone. This is an expected result of the microcracking enhancement on the reaction rate due to the severe stress concentration in front of the crack tip. Interestingly, it is also noticed that a pronounced localization of accumulated mass removal has developed in proximity to the crack tip point, for instance, at $t = 600$ h (at a distance of around five folds of the mesh size), suggesting a possible micro-banding that nucleates from the imposed initial heterogeneity. This micro-localization phenomenon is also evident in the evolution of the radial distribution of the deviatoric stress along the crack propagation direction, as shown in Fig. 13b. At $t = 600$ h, a drop in the deviatoric stress distribution profile in close proximity to the crack tip arises, suggesting a localized softening in the chemically enabled yield zone.

We compare the radial distribution of the accumulated mass removal and the counterpart of the deviatoric stress along three directions ($\theta = 0, \pi/4, \pi/2$). We first plot the comparison after the contained macroscopic crack is subject to concomitant pressurization and acidizing for 600 h, as shown in Fig. 14. The enhancement on chemical mass removal is only significant at the crack propagation direction, while at the direction of $\theta = \pi/4$ and the direction perpendicular to the crack propagation ($\theta = \pi/2$) there is negligible damage enhancement (see Fig. 14a) suggesting little micro-cracking activities even in the region close to the blunt-tip. For the stress field, as shown in Fig. 14b, the distribution of the deviatoric stress along the direction $\theta = \pi/4$ and $\pi/2$ after 600 h is nearly identical to the case where homogeneity is assumed (see Fig. 4). At $\theta = 0$, it is observed that the maximum value of the deviatoric stress decreases slightly, and if we zoom into the plasticity region we notice that minimum of the deviatoric stress shifts from the inner boundary of the crack tip (as shown in Fig. 4) to a certain distance away from the tip (as shown in the inset of Fig. 14b), corresponding to the localized chemical mass removal in Fig. 14a.

We further plot the time evolution of the distribution of accumulated mass removal and the counterpart of the deviatoric stress, respectively, along the surface of the blunt crack tip at $\theta \in [-\pi/2, \pi/2]$, as shown in Fig. 15a, b. With the imposed initial imperfection, the distribution fluctuates outlining the trend of a prominent growth of the chemical mass removal spanning from $\theta = -0.2\pi$ to $\theta = 0.2\pi$ arises, as evident at $t = 600$ h in Fig. 15a. Sporadic values are exceptionally high close to the crack propagation direction, due to the two-way chemo-mechanical feedback amplified around the imposed initial imperfections. These are expected to assist the macroscopic extension of the single crack, along $\theta = 0$. The prominent growth in chemical mass removal essentially origins from the intense micro-cracking activities and hence highlights the chemically enabled plasticity region in front of the crack tip. Inside the yield zone of $\theta \in [-0.2\pi, 0.2\pi]$, the chemical softening effect progresses with time, and a significant fluctuation in the distribution of the deviatoric

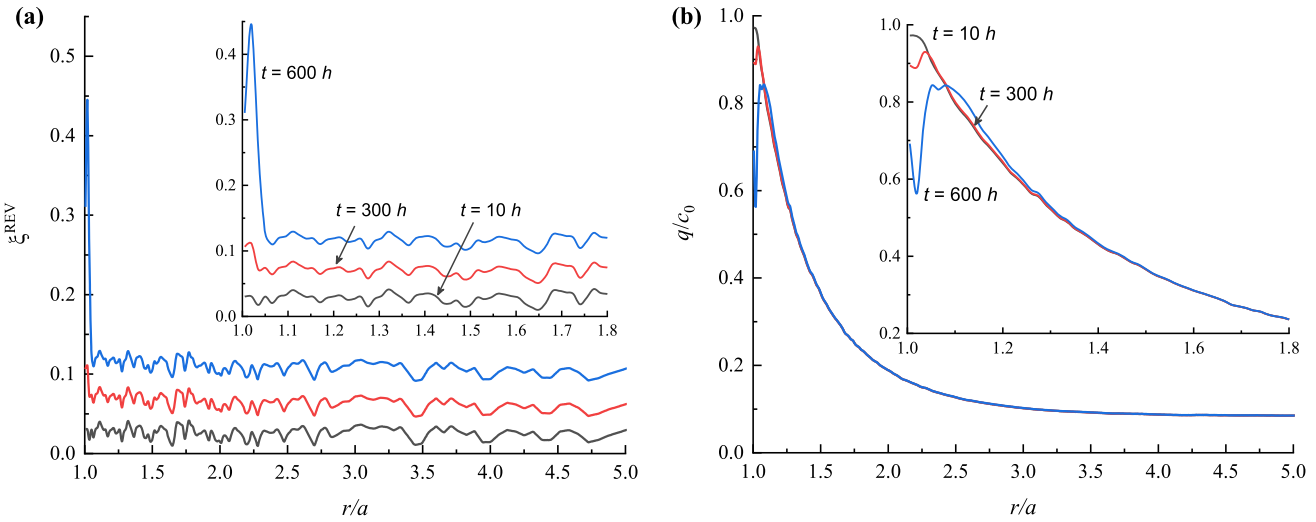

Fig. 13 Evolution of the distribution of **a** accumulated mass removal and **b** deviatoric stress normalized by the initial cohesion along the radius at propagation direction ($\theta = 0$), upon 10, 300, and 600 h of exposure for cases with the consideration of heterogeneity on intrinsic material property

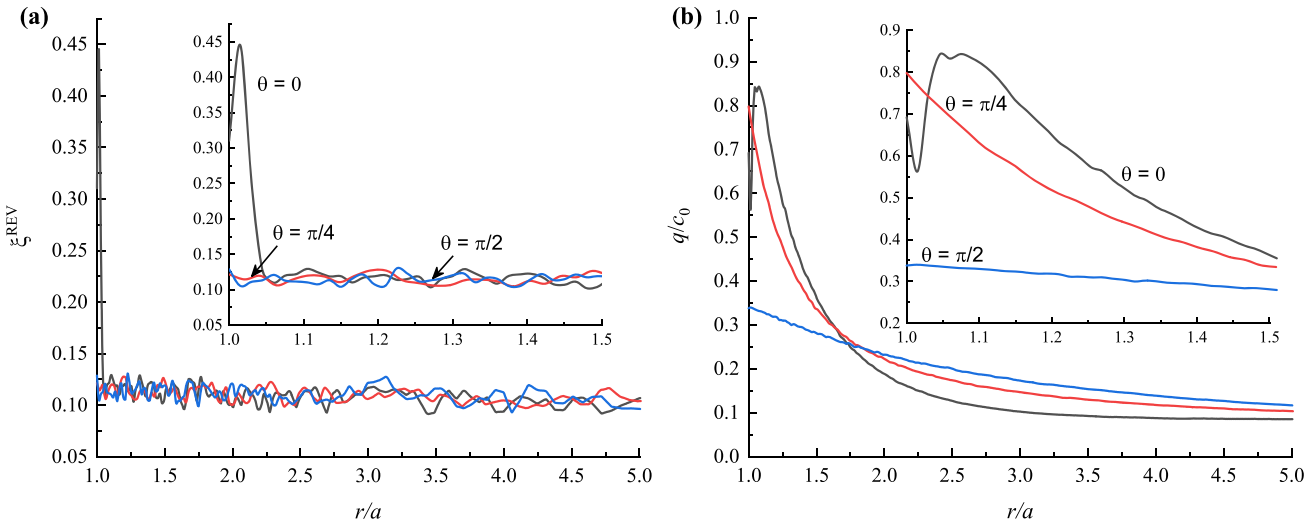

Fig. 14 Distribution of **a** accumulated mass removal and **b** deviatoric stress normalized by the initial cohesion along radius at three trajectories (θ = 0, π/4, π/2) at a timestep with 600 h of exposure

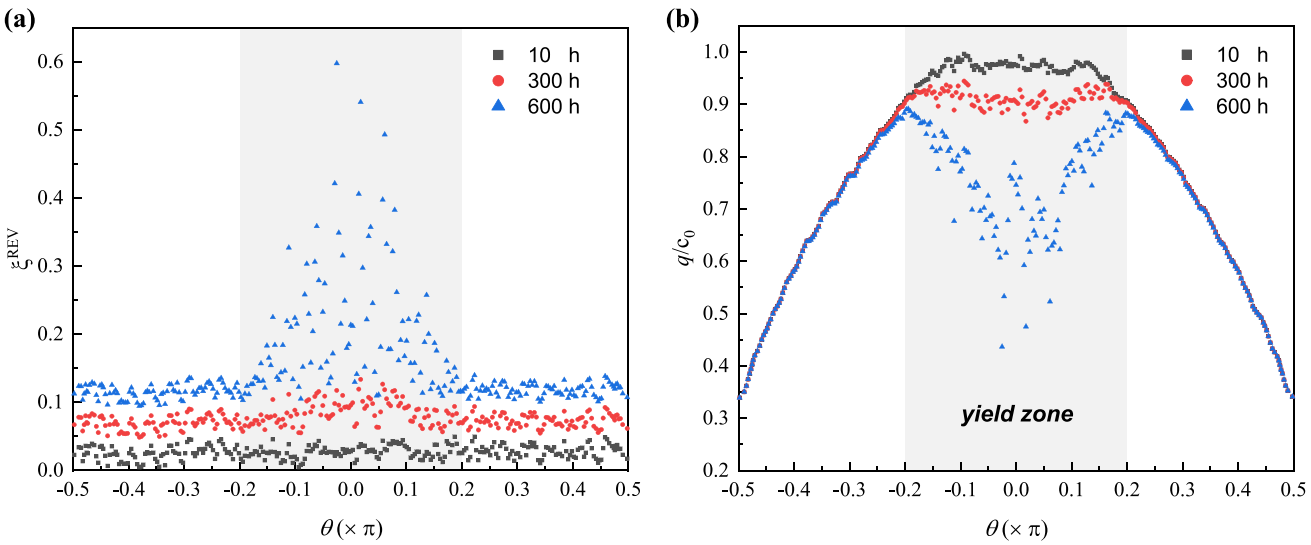

Fig. 15 Distribution of **a** accumulated mass removal and **b** deviatoric stress normalized by the initial cohesion along crack tip surface ($\theta \in [-\pi/2, \pi/2]$) upon 10, 300, and 600 h of exposure

stress exhibits, again around the crack propagation direction as demonstrated in Fig. 15b.

How the magnitude of the initial imperfection affects the propagation of the macroscopic crack is illustrated in Fig. 16. We compare three cases with the imposed initial imperfection represented by $\xi_0^{\mathrm{loc}} = 0$, [0, 0.025], and [0, 0.05], respectively. Compared to the homogeneous case ($\xi_0^{\mathrm{loc}} = 0$) where the initial mechanical properties are uniformly distributed within the process zone, with an initial imperfection implemented as $\xi_0^{\mathrm{loc}} \in [0, 0.025]$ the crack propagation accelerates in the presence of the same chemical environment ($\mathrm{pH}_a = 5.3$). When the initial imperfection is increased to $\xi_0^{\mathrm{loc}} \in [0, 0.05]$, corresponding to an increased level of microstructural heterogeneity in the rock, the acceleration of the macroscopic hydro-pressurized crack propagation under acidizing is enhanced. As shown in Fig. 16, after 650 h of exposure, with $\xi_0^{\mathrm{loc}} \in [0, 0.05]$ the propagation of the macroscopic crack is approximately one order of magnitude further into the softening rock compared to the reference case of homogeneity $\xi_0^{\mathrm{loc}} = 0$.

For this case, a visible jump in the acceleration is noticed at around $t = 580$ h when micro-bands start to develop inside the chemically enabled plasticity zone. As shown in the magnified deviatoric strain patterns in front of the crack tip at $t = 650$ h, the initial imperfection acts as seeds allowing the deformation in the yield zone spanning

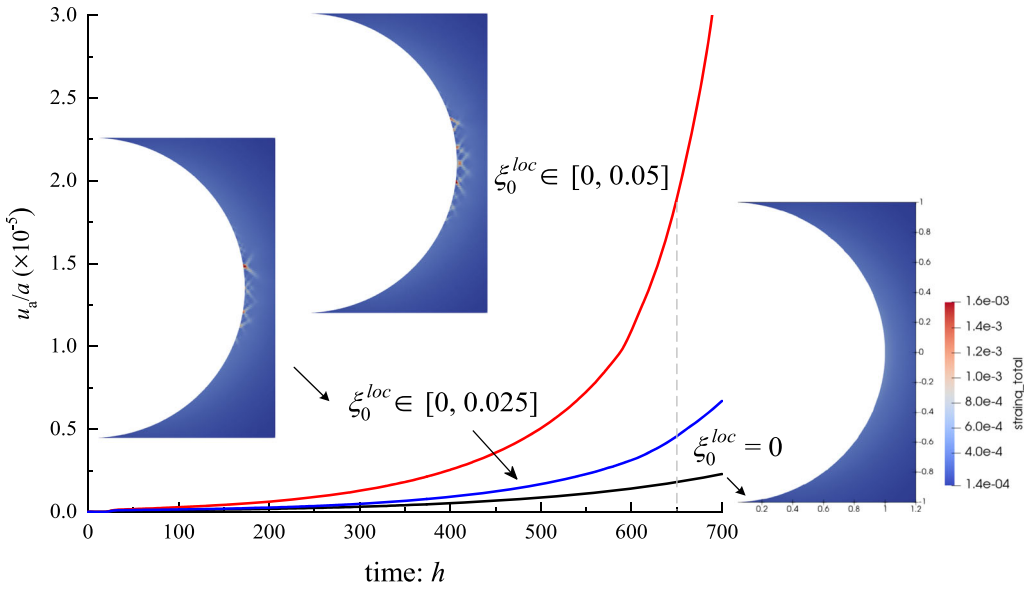

Fig. 16 Time evolution of the crack propagation for cases with various degrees of preset heterogeneity on the intrinsic material property by scopes of 0, [0, 0.025] and [0, 0.05], respectively. Patterns of deviatoric strain (total strain) near the crack tip at a timestep of 650 h' acid exposure are depicted with the emergence of shear localization near the crack tip in heterogeneity cases

$\theta \in [-0.2\pi, 0.2\pi]$ (as Fig. 15 indicates) to self-organize into a network of micro-bands.

5 Conclusions

This paper presents an investigation on how a macroscopic blunt-tip crack propagates into a carbonate rock subject to fluid pressurization and acidizing from the crack opening. A reactive-chemo-mechanical model is introduced taking into account the constitutive considerations for carbonate rocks in a reactive environment in both the elastic and plastic domains, as well as acid delivery in front of the crack tip being coupled to micro-cracking activities. A two-dimensional subcritical propagation of a macroscopic crack is numerically investigated using a finite element implementation built in the MOOSE framework. Sensitivity studies on the intensity of the chemical environment and the damage-enhancement coefficient are incorporated. The role of initial imperfections in the carbonate rock that relates to the inherent microstructural variations is also investigated. The main findings are summarized as follows:

(1) The numerical results show that the chemical process (here calcite dissolution) plays a crucial role driving the subcritical propagation of the single crack under fixed mechanical boundary conditions. Strong nonlinearity appears in the radial distribution of the deviatoric stress, resulting from the severe stressing in the vicinity of the crack tip, interacting with the damage-affected chemical mass removal process. The mineral dissolution is most enhanced along the crack propagation direction due to a concentrated irreversible deformation.

(2) The plot of crack propagation velocity versus stress intensity factor (Fig. 11) shows a three-region development which is typical for a single tensile crack subject to a reactive environment. In Region I, the crack growth in an early stage is mainly controlled by the chemical reaction rate; In Region II, the reaction is slowed down while microcracking starts to develop in front of the crack tip which facilitates the acid delivery; In Region III, the crack propagation exhibits a prominent acceleration due to an elevated level of local acidity and a micro-fracturation enhancement. The above-described hypothesis is further supported by Fig. 12.

(3) Considering an initial imperfection in the rock material, significant fluctuation appears in the profile of both the chemical and mechanical fields, with an outstanding trend of growth in mass removal (and hence chemical softening) concentrated in the close proximity of the crack tip. The propagation of the macroscopic crack is thereby accelerated. A secondary acceleration of the subcritical macroscopic crack emerges when a network of micro-bands self-organizes inside the chemically enabled plasticity zone spanning $\theta \in [-0.2\pi, 0.2\pi]$ in front of the macroscopic crack tip.

Acknowledgements The support by Research Grant Council of Hong Kong (ECS 27203720, GRF 17206521) is acknowledged.

Data availability Data will be made available on reasonable request.

Declarations

Conflict of interest There is no conflict of interest between the authors.

References

1. Airy GB (1863) IV. On the strains in the interior of beams. Philos Trans R Soc Lond 153:49–79. https://doi.org/10.1098/rstl.1863.0004
2. Anderson TL (2017) Fracture mechanics: fundamentals and applications. CRC Press
3. Atkinson BK (1984) Subcritical crack growth in geological materials. J Geophys Res Solid Earth 89(B6):4077–4114. https://doi.org/10.1029/JB089iB06p04077
4. Atkinson BK, Meredith PG (1981) Stress corrosion cracking of quartz: a note on the influence of chemical environment. Tectonophysics 77(1–2):T1–T11. https://doi.org/10.1016/0040-1951(81)90157-8
5. Atkinson C, Eshelby J (1968) The flow of energy into the tip of a moving crack. Int J FractMech 4(1):3–8. https://doi.org/10.1007/BF00189137
6. Bathurst RG (1961) Diagenetic fabrics in some British Dinantian limestones. Geol J 2(1):11–36. https://doi.org/10.1002/gj.3350020103
7. Borja RI, Chen W, Odufisan AR (2023) A constitutive framework for rocks undergoing solid dissolution. J Mech Phys Solids 173:105198. https://doi.org/10.1016/j.jmps.2023.105198
8. Carpinteri A, Paggi M (2009) A unified interpretation of the power laws in fatigue and the analytical correlations between cyclic properties of engineering materials. Int J Fatigue 31(10):1524–1531. https://doi.org/10.1016/j.ijfatigue.2009.04.014
9. Chen W, Zhao Y, Borja RI (2023) Solid–fluid interaction in porous materials with internal erosion. Acta Geotech. https://doi.org/10.1007/s11440-023-01906-4
10. Ciantia MO, Castellanza R, Crosta GB, Hueckel T (2015) Effects of mineral suspension and dissolution on strength and compressibility of soft carbonate rocks. Eng Geol 184:1–18. https://doi.org/10.1016/j.enggeo.2014.10.024
11. Ciantia MO, Castellanza R, di Prisco C (2015) Experimental study on the water-induced weakening of calcarenites. Rock Mech Rock Eng 48(2):441–461. https://doi.org/10.1007/s00603-014-0603-z
12. Ciantia MO, Hueckel T (2013) Weathering of submerged stressed calcarenites: chemo-mechanical coupling mechanisms. Géotechnique 63(9):768–785. https://doi.org/10.1680/geot.SIP13.P.024
13. Desrues J, Viggiani G (2004) Strain localization in sand: an overview of the experimental results obtained in Grenoble using stereophotogrammetry. Int J Numer Anal Methods Geomech 28(4):279–321. https://doi.org/10.1002/nag.338
14. Fredd CN, Fogler HS (1998) Influence of transport and reaction on wormhole formation in porous media. AIChE J 44(9):1933–1949. https://doi.org/10.1002/aic.690440902
15. Freiman SW, Wiederhorn SM, Mecholsky J, John J (2009) Environmentally enhanced fracture of glass: a historical perspective. J Am Ceram Soc 92(7):1371–1382. https://doi.org/10.1111/J.1551-2916.2009.03097.X
16. Freund L (1972) Energy flux into the tip of an extending crack in an elastic solid. J Elast 2(4):341–349. https://doi.org/10.1007/BF00045718
17. Gaston D, Newman C, Hansen G, Lebrun-Grandié D (2009) MOOSE: a parallel computational framework for coupled systems of nonlinear equations. Nucl Eng Des 239(10):1768–1778. https://doi.org/10.1016/j.nucengdes.2009.05.021
18. Griffith AA (1921) VI. The phenomena of rupture and flow in solids. Philos Trans R Soc Lond Ser A Contain Pap Math Phys Charact 221(582–593):163–198
19. Guo R, Hueckel T (2013) Growth of polymer microstructures between stressed silica grains: a chemo-mechanical coupling. Géotechnique 63(4):322–330. https://doi.org/10.1680/geot.SIP13.P.021
20. Guo R, Hueckel T (2015) Silica polymer bonding of stressed silica grains: an early growth of intergranular tensile strength. Geomech Energy Environ 1(1):48–59. https://doi.org/10.1016/j.gete.2015.02.002
21. Hu LB, Hueckel T (2007) Coupled chemo-mechanics of intergranular contact: toward a three-scale model. Comput Geotech 34(4):306–327. https://doi.org/10.1016/j.compgeo.2007.02.009
22. Hu M, Regenauer-Lieb K (2018) Entropic limit analysis applied to radial cavity expansion problems. Front Mater 5:1–10. https://doi.org/10.3389/fmats.2018.00047
23. Hu M, Schrank C, Regenauer-Lieb K (2020) Cross-diffusion waves in hydro-poro-mechanics. J Mech Phys Solids 135:103632. https://doi.org/10.1016/j.jmps.2019.05.015
24. Hu M, Sun Q, Schrank C, Regenauer-Lieb K (2022) Cross-scale dynamic interactions in compacting porous media as a trigger to pattern formation. Geophys J Int 230(2):1280–1291. https://doi.org/10.1093/gji/ggac115
25. Hu M, Veveakis M, Poulet T, Regenauer-lieb K (2017) The role of temperature in shear instability and bifurcation of internally pressurized deep boreholes. Rock Mech Rock Eng 50(11):3003–3017. https://doi.org/10.1007/s00603-017-1291-2
26. Hu MM, Hueckel T (2013) Environmentally enhanced crack propagation in a chemically degrading isotropic shale. Geotechnique 63(4):313–321. https://doi.org/10.1680/geot.SIP13.P.020
27. Hu MM, Hueckel T (2019) Modeling of subcritical cracking in acidized carbonate rocks via coupled chemo-elasticity. Geomech Energy Environ 19:100114. https://doi.org/10.1016/j.gete.2019.01.003
28. Hutchinson J (1968) Singular behavior at the end of a tensile crack in a hardening material. J Mech Phys Solids 16(1):13–31. https://doi.org/10.1016/0022-5096(68)90014-8
29. Ip SCY, Borja RI (2023) Modeling heterogeneity and permeability evolution in a compaction band using a phase-field approach. J Mech Phys Solids 181:105441. https://doi.org/10.1016/j.jmps.2023.105441
30. Irwin GR (1957) Analysis of stresses and strains near the end of a crack traversing a plate. J Appl Mech. https://doi.org/10.1115/1.4011547
31. Johnson W, Sowerby R, Venter RD, Kobayashi S (1983) Plane-strain slip-line fields for metal-deformation processes. J Appl Mech 50(3):702–702. https://doi.org/10.1115/1.3167124

32. Neuner M, Abrari Vajari S, Arunachala PK, Linder C (2023) A better understanding of the mechanics of borehole breakout utilizing a finite strain gradient-enhanced micropolar continuum model. Comput Geotech 153:105064. https://doi.org/10.1016/j.compgeo.2022.105064
33. Pardoen B, Pont SD, Desrues J, Bésuelle P, Prêt D, Cosenza P (2018) Heterogeneity and variability of clay rock microstructure in a hydro-mechanical double scale fem × fem analysis. In: Giovine P, Mariano PM, Mortara G (eds) Micro to MACRO mathematical modeling in soil mechanics. Springer, pp 247–256
34. Perzyna P (1966) Fundamental problems in viscoplasticity. In: Chernyi GG et al (eds) Advances in applied mechanics. Elsevier, pp 243–377
35. Poulet T, Paesold M, Veveakis M (2017) Multi-physics modeling of fault mechanics using REDBACK: a parallel open-source simulator for tightly coupled problems. Rock Mech Rock Eng 50(3):733–749. https://doi.org/10.1007/s00603-016-0927-y
36. Poulet T, Veveakis M (2016) A viscoplastic approach for pore collapse in saturated soft rocks using REDBACK: an open-source parallel simulator for rock mechanics with dissipative feedbacks. Comput Geotech 74:211–221. https://doi.org/10.1016/j.compgeo.2015.12.015
37. Qu J, Bassani J (1993) Interfacial fracture mechanics for anisotropic bimaterials. J Appl Mech. https://doi.org/10.1115/1.2900810
38. Rahman M (2008) Constrained hydraulic fracture optimization improves recovery from low permeable oil reservoirs. Energy Sour Part A 30(6):536–551. https://doi.org/10.1080/15567030601082035
39. Rice JR (1968) A path independent integral and the approximate analysis of strain concentration by notches and cracks. J Appl Mech 35(2):379–386. https://doi.org/10.1115/1.3601206
40. Schapery RA (1984) Correspondence principles and a generalized J-integral for large deformation and fracture analysis of viscoelastic media. Int J Fract 25(3):195–223. https://doi.org/10.1007/BF01140837
41. Shahin G, Desrues J, Pont SD, Combe G, Argilaga A (2016) A study of the influence of REV variability in double-scale FEM × DEM analysis. Int J Numer Methods Eng 107(10):882–900. https://doi.org/10.1002/nme.5202
42. Shahin G, Viggiani G, Buscarnera G (2020) Simulating spatial heterogeneity through a CT-FE mapping scheme discloses boundary effects on emerging compaction bands. Int J Solids Struct 206:247–261. https://doi.org/10.1016/j.ijsolstr.2020.08.016
43. Sjöberg EL (1976) A fundamental equation for calcite dissolution kinetics. Geochim Cosmochim Acta 40(4):441–447. https://doi.org/10.1016/0016-7037(76)90009-0
44. Sjöberg EL, Rickard DT (1984) Temperature dependence of calcite dissolution kinetics between 1 and 62 °C at pH 2.7 to 8.4 in aqueous solutions. Geochim Cosmochim Acta 48(3):485–493. https://doi.org/10.1016/0016-7037(84)90276-X
45. Tada R, Maliva R, Siever R (1987) A new mechanism for pressure solution in porous quartzose sandstone. Geochim Cosmochim Acta 51(9):2295–2301. https://doi.org/10.1016/0016-7037(87)90282-1
46. Tang X, Hu M (2023) A reactive-chemo-mechanical model for weak acid-assisted cavity expansion in carbonate rocks. Rock Mech Rock Eng 56:515–533. https://doi.org/10.1007/s00603-022-03077-2
47. Wiederhorn S (1967) Influence of water vapor on crack propagation in soda-lime glass. J Am Ceram Soc 50(8):407–414. https://doi.org/10.1111/j.1151-2916.1967.tb15145.x